CEAS Aeronautical Journal
https://doi.org/10.1007/s13272-026-00945-3

ORIGINAL PAPER

Comparative assessment of propeller noise prediction methods against flyover data

Vincent Domogalla[1] · **Antje Feldhusen-Hoffmann**[2] · **Jatin Manghnani**[2]

Received: 14 October 2025 / Revised: 22 January 2026 / Accepted: 26 January 2026

Abstract

This study presents a noise prediction toolchain for propeller aircraft, specifically designed for application in early preliminary design phases. Thereby, novel propeller aircraft designs can be provided with low-noise capabilities, and optimal landing and takeoff trajectories as well as the impact on the communities of such aircraft can be investigated. Two aerodynamic modeling approaches for propeller load prediction are compared: a simple blade element method and a full 3D aerodynamic model. This data is furthermore processed and provided as input for the noise prediction. Based on these results, the study evaluates tonal noise predictions from Hanson's and Farassat's models against flyover noise measurements of a Do 228 aircraft under various operating conditions. The comprehensive study assesses model performances across different velocity regimes. Key findings reveal that unweighted maximum sound pressure levels increase with both airspeed and rotational speed. Flight speed significantly influences the radial position of the thrust peak, shifting it outward from approximately 65–85% of the blade radius as speed increases. However, this outward shift does not significantly affect tonal noise emission. While both noise models successfully predict the velocity trend, simulations consistently underpredict noise levels by 3 dB to 5 dB compared to experimental data.

Keywords Propeller · Noise · PANAM · Flyover · BEMT · Loading

Acronyms

AGL	Above ground level
BEMT	Blade element momentum theory
BET	Blade element theory
CFD	Computational fluid dynamics
CPACS	Common parametric aircraft configuration schema
DLR	German Aerospace Center
Do 228	Dornier 228-101 (D-CODE) research aircraft of DLR
FW-H	Ffowcs Williams - Hawkings equation
GPS	Global positioning system
ICAO	International Civil Aviation Organization
INS	Inertial navigation system
RPM	Revolutions per minute
SAF	Sustainable aviation fuel
TAS	True air speed
VFM	Vortex filament method
VLES	Very large eddy simulation
VPM	Vortex particle method

Symbols Greek

α	Angle of attack in °
β	Twist angle in °
η	Efficiency
Φ	Lateral emission angle in °
ϕ	Local flow angle in °
ρ	Density in $\mathrm{kg/m^3}$
φ	Sweep angle in °
Θ	Longitudinal emission angle in °

✉ Vincent Domogalla
vincent.domogalla@dlr.de

Antje Feldhusen-Hoffmann
antje.feldhusen-hoffmann@dlr.de

Jatin Manghnani
jatin.manghnani@dlr.de

[1] DLR, German Aerospace Center, Bunsenstr. 10, Göttingen 37073, Germany

[2] DLR, German Aerospace Center, Carlo-Schmid-Str. 12, Würselen 52146, Germany

Published online: 13 February 2026

Symbols Latin

B	Number of blades
c	Chord length in m
c_d	Drag coefficient
c_l	Lift coefficient
f	Frequency in Hz
J	Advance ratio ($= v/(nD)$)
L	Sound pressure level in dB ($p_{ref} = 20\mu Pa$)
n	Rotational speed in $1/\mathrm{min}$
Q	Torque in Nm
R	Blade radius (tip) in m
r	Local radius in m
T	Thrust in N
t	Thickness in m
t	Time in s
v	Velocity in m/s
W	Local total velocity in $\mathrm{m/s}$
W_a	Local axial velocity in $\mathrm{m/s}$
W_t	Local tangential velocity in $\mathrm{m/s}$
x, y, z	Cartesian coordinates in m

Tools

APSIM	Acoustics prediction system based on integral method, DLR,
FLIPNA	Flightpath for noise analysis, DLR,
PANAM	Parametric aircraft noise assessment module, DLR,
QPROP	Blade element vortex theory code, MIT,
UPM	Unsteady panel method, 3D unsteady panel method, DLR,
xflr5	Analysis tool for airfoils, wings and planes operating at low Reynolds numbers, André Deperrois and Matthieu Scherrer,

Subscripts

25	Unit measured at the quarter chord
max	Maximum
$prop$	Propeller
rel	Relative

1 Introduction

Demanded by the EU's FlightPath 2050 program, reduction of the environmental impact is the paramount design driver of future aircraft designs. Especially the mitigation of CO_2 and NO_x and noise is a key element [1]. Using sustainable aviation fuel (SAF) as a drop-in replacement can help to reduce the climate impact in terms of CO_2, but costs are predicted to be significantly higher than for fossil fuels [2, 3]. Therefore, a reduction in fuel consumption becomes even more important. Recently, DLR showed that a reduction in cruise speed combined with a lower cruise altitude can contribute to this goal [3]. The comparison showed that propeller-driven aircraft can leverage their higher efficiency in this flight regime, leading to a reduction of fuel consumption on mid-range routes by 15–30%.

Most of the noise at major airports originates from turbofan-driven mid-range aircraft like the Airbus A320 and Boeing B737, which dominate traffic numbers [4, 5]. However, propeller engines generate more low-frequency noise, which affects perception [6] and propagation [7] differently. Introducing a new generation of propeller aircraft for mid-range applications potentially alters the noise impact of airports on surrounding communities. To accurately assess future noise scenarios around airports, noise prediction tools must include propeller noise modeling. Furthermore, the behavior of the implemented propeller noise model in interaction with other sources like airframe noise needs to be assessed.

Ideally, the noise impact of novel aircraft concepts is already considered by aircraft manufacturers during the conceptual phase, ensuring maximum impact and cost efficiency. Therefore, it is important to develop the capabilities of propeller noise prediction to incorporate them into preliminary design workflows.

Working towards this goal, DLR conducted different noise measurement campaigns of small turboprop aircraft in 2022 and 2023. The campaigns aimed to generate a reliable data set for validation and research [8, 9]. Furthermore, the current process for aircraft noise assessment tool chains at German Aerospace Center (DLR) is extended to predict propeller noise. A preliminary status of the toolchain is described by Manghnani et al. [10], and applied to a low speed flyover case with the Dornier 228-101 (Do 228) . The work also describes how the toolchain can be extended for external source models, such as the Ffowcs Williams- Hawkings equation (FW-H) solver acoustics prediction system based on integral method. The comparison of simulation to measurement shows underprediction of ground noise levels, for the A-weighted and unweighted maximum sound pressure level. In addition to this, Hon's assessment investigates the second measurements campaign with the Cessna F406 and follows a simplified approach for propeller noise prediction [9]. Instead of relying on radial blade loadings as input, the effective radius assumption is used. This was introduced by Gutin [11] and assumes a point force applied at a single radial station of the blade as a representative noise source. Varying the effective radius showed significant influence on the predicted noise. Therefore, it is crucial to choose a representative radius.

Building on the research by Manghnani et al. [10] and Hon et al. [9], this work details the development of the applied toolchain. The constant underprediction of propeller

noise for both cases require further investigation. The work of Hon indicates an important influence of the blade loading when using the effective radius assumption [9]. Therefore, this study focuses on the effect of realistic loading distributions on noise emission. It also investigates how the load distributions are affected by flight speed, propeller rotational speed, and the applied aerodynamic method (QPROP, UPM).

Furthermore, this study evaluates the effect of flight and propeller rotation speed on ground noise levels and investigates whether a higher fidelity approach (UPM / APSIM) improves the agreement between simulation and experiment. Measurement results are compared for flight speeds between $110\,\mathrm{kts}$ and $190\,\mathrm{kts}$ in clean configuration. The recordings were taken from the Do 228 dataset [8] already used by Manghnani et al. [10]. The assessment focuses on mean L_{max} of each operating condition, comparing simulated maximum noise levels on the ground for selected test points at both revolutions per minute (RPM) settings ($1527\,1/\mathrm{min}$ and $1591\,1/\mathrm{min}$).

The aim of this work is to gain deeper understanding of the observed deviations of the predicted and measured L_{max} and to optimize the prediction process by investigating the possible limits of the applied process in terms of the aerodynamic input and its implications on noise prediction.

2 Literature review

2.1 Influence of operating conditions on radial blade loading

Nallasamy et al. investigate the influence of different blade angles, i.e., thrust conditions with a constant advance ratio for high-speed propeller [12]. Shape and peak of the radial thrust and torque distribution are almost independent of the applied thrust and only a slight inboard movement is observed (85–82.5%).

2.2 Tonal propeller noise models

During the 1980 s, two prominent analytical models for propeller noise prediction were developed and still widely used today. Hanson developed its helicoidal surface theory [13] and Farassat's his equations 1 and 1A [14]. Both models are derived from FW-H [15]. The generalized acoustic source functions, which typically require unsteady or steady, volume-resolved flow quantities as input, are replaced by simplified formulations that can be obtained from steady flow simulations and do not require volume-resolved quantities. Although both authors also developed solutions to include quadrupole volume sources, their contribution can be neglected at low tip Mach numbers and noise predictions are assembled by monopole and dipole sources only [13, 16]. This simplification holds until the propeller blade sections approach the critical Mach number [17]. The different sources can be attributed to blade thickness noise (monopole) and blade loading noise (dipole). Notably, the models differ in how the source functions are solved. Hanson developed and refined a frequency-domain approach [18, 19]. Farassat solves the source function in the time domain.

The research on tonal propeller noise mostly focuses on comparative studies, where wind tunnel measurements are compared to numerical results. Especially the combination of aerodynamic and aeroacoustic methods is subject of active research. Bergmann et al. [20] and Zawodny et al. [21] investigate small rotors at low Reynolds numbers, and Hambrey et al. [22] investigate high-speed rotors. There is no clear tendency, which aeroacoustic model performs best, and performance is case-dependent. Nevertheless, using high-fidelity methods to predict the aerodynamic loading such as CFD does not improve the acoustic results of isolated rotors in steady conditions.

2.3 Influence of radial blade loading on noise

Initial assessments of the influence of radial blade loading were already conducted at the time when the tonal propeller noise models were developed. Succi [23] investigated the effect on noise by manipulating the twist distribution of a predefined propeller, a 2-bladed McCauley 1C160, while keeping the planform untouched. Moving the loading peak inboard from 80 to 60% of the blade radius results in a reduction of $1.6\,\mathrm{dB}$ and $4.2\,\mathrm{dBA}$ while similarly reducing the efficiency by 3.9%. The comparable small reduction in noise is explained by portion of the load that still remains at the tip. A similar study for different propeller tip configurations (straight, proplet, bi-blade) was conducted by Miller and Sullivan [24], showing that the trends observed by Succi et al. hold true in case of exotic tip treatments as well. The investigation of Hon et al., who used the simplified radius assumption, showed a significant impact of the selected effective radius on noise [9]. The authors investigated a Reims Cessna F406 with two five bladed MTV-27 propellers. These propellers are quite similar to the propellers investigated in the present work, but have a smaller diameter of $2.2\,\mathrm{m}$. In this case, a variation of r_{eff} from 60 to 80% results in a difference of $10\,\mathrm{dB}$.

2.4 Flyover noise predictions

Recent publications to flyover noise measurements or predictions are rarely available. A recent effort similar to this work was published by Yunus et al. [25]. In their study, they

investigated the tonal noise of a two-seat single-engine electric aircraft, the Pipistrel Velis Electro, under various operating conditions. The authors combine a blade element theory (BET) with Hanson's model for propeller noise prediction and compare the results to high-fidelity computational fluid dynamics (CFD) and measurements. This approach is similar to the one used in this work, but focuses on propeller noise only. The simulation results showed satisfactory agreement with measurements below the flight path. Levels below the flight are matched within a range of 1.5 dB. Another prediction of flyover noise was made by Grande et al. [26]. They compared ground noise measurements to high-fidelity results using a Lattice-Boltzmann/very large eddy simulation (VLES) simulation coupled to a FW-H solver. Similar to Yunus et al. [25], they focused on tonal propeller noise only. The investigated aircraft was the Beechcraft King Air 350, a twin-engine turboprop aircraft. The tonal noise could be simulated within 2 dB accuracy of the measurements.

3 Toolchain development

The toolchain used for this and for previous studies is developed to integrate into the established noise prediction toolchain of DLR. It uses parametric aircraft noise assessment module [27] as noise prediction tool, accompanied by flightpath for noise analysis [28] for calculating the aircraft trajectory, and by an interface to the common parametric aircraft configuration schema (CPACS) data format. This is a data exchange format, which contains all important information about an aircraft and enables for a defined interface to arbitrary aircraft design tools.

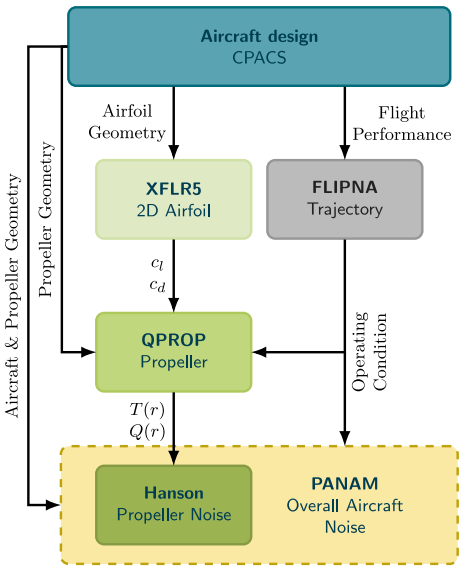

Fig. 1 Schematics of the propeller noise simulation toolchain for PANAM

3.1 Toolchain requirements

Various requirements can be derived from integration into the existing tool chain and application for optimization processes. The toolchain must compute third-octave-band noise levels with emphasis on tonal components, resolving the blade-passing frequency and its harmonics. This has to be achieved by only relying on data available during early design phases, enabled through the CPACS data format [29]. Furthermore, short computation times are essential for an efficient application in design optimization loops. The correct prediction of trends is more important than perfect replication of measurement data. Information about performance and geometry are subject to high uncertainties, during early design phases. But it is essential to predict the correct trends from the beginning on to avoid costly re-engineering in later design phases. An overall accuracy comparable to the turbofan noise toolchain, i.e., within 2 dB to 3 dB [27], is desirable but challenging. Unducted propellers are much more sensitive to environmental influences and installation effects compared to ducted turbofans.

3.2 Toolchain

The scheme of the developed toolchain is depicted in Fig.1. Starting point of the toolchain is the aircraft design provided by the design tool as CPACS file. Here, aircraft engine and aerodynamic performance have to be provided along with geometry of the aircraft itself, especially the high lift system, and the propeller. A detailed overview about the applied tools in this work is given in section 5.1.

The CPACS dataset defines the propeller blade as multiple 2D airfoil sections, similar to how BET considers a propeller blade. Depending on the data quality, a geometry pre-processing is necessary to create 2D airfoil sections suitable for the computation in xflr5 [30]. This is a 2D prediction code, similar to XFOIL and used to compute lift and drag polars for each airfoil section at different Reynolds and Mach numbers.

This aerodynamic dataset is now used to calculate the propeller aerodynamics. In general, every method based on the BET can be used and achieves similar results [31]. In this case with QPROP is used. This model is capable to predict propeller thrust and torque at a selected operating condition, i.e., thrust or power, RPM. If the aircraft uses a constant speed propeller, blade pitch has either to be defined as well, or can be inferred by optimizing the blade pitch for a minimum power condition. The propeller is modeled as an isolated propeller with axial inflow. Goyal et al. [32] demonstrated that the mean load distribution does not change significantly with angle of attack. Therefore, a single mean load distribution computed from the averaged operating

condition is used throughout the whole trajectory and only the absolute thrust is varied. This approach might have to be adapted when simulating landing and takeoff trajectories, where operating conditions vary significantly with time, or when including unsteady blade loadings.

The operating conditions required by the blade element momentum theory (BEMT) model are taken from the trajectory. This is calculated with FLIPNA based on aerodynamic and engine performance of the aircraft, if not provided with the aircraft dataset. The trajectory contains the aircraft position, attitude, power setting (thrust, RPM) and high-lift configuration, along with landing gear configuration.

The trajectory, together with aircraft geometry, propeller geometry, and propeller loading is now used by PANAM to predict the ground noise at defined microphone positions. Optionally, the calculated noise level can then be fed, among other parameters, into a multidisciplinary optimization loop to obtain an aircraft design optimized for noise. As applied previously, e.g., in [10], PANAM possesses the ability to include external noise sources. In the present work, this interface is used to incorporate the FW-H solver APSIM. This setup is shown in Fig.2. PANAM uses noise levels, computed in 1/3 octave bands as input. These source noise levels have to be pre-computed at a hemisphere enclosing the aircraft. APSIM calculates the source noise based on the spatial pressure field at the blade surface. The pressure field is provided from the 3D unsteady panel solver UPM using the 3D propeller geometry. The geometry can be assembled from the 2D sections provided in the CPACS dataset. Besides geometry information, UPM also requires the operating condition. Computational times of this approach are orders of magnitude higher, compared to the BEMT toolchain. Therefore, this approach is currently limited to assess single operating condition only. The important advantage of this approach is that it covers complex 3D flows and can include aerodynamic installation effects as well.

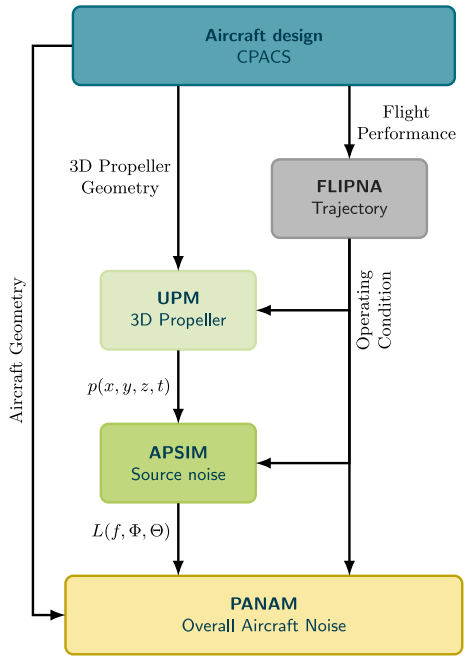

Fig. 2 Schematics of the propeller noise simulation toolchain for PANAM with the external FW-H source model APSIM

Fig. 3 DLR research aircraft Do 228, Credit: DLR (CC BY-NC-ND 3.0)

4 Measurement

The Do 228 aircraft (Fig. 3) performed flyovers over the runway at constant operating settings 2 km before and 2 km after the measurement stations [8]. The flyover altitude was 500 ft above ground level (AGL). Also, low altitude flyovers at 30 ft AGL have been done, but are not part of the analysis presented in this study. The test matrix contained overall 40 test points which were repeated three times in order to assure some redundant measurements. For each flyover, the positions of flaps and gears, the RPM of the propeller, and the speed of the aircraft were varied. In the presented study, only the clean configuration is considered. The resulting noise for RPMs of 96% and 100% of the propeller's nominal rotational speed is recorded for five aircraft speeds, i.e., 110 kts, 130 kts, 150 kts, 170 kts, and 190 kts.

The acoustic recording system comprised overall 16 microphones mounted on different heights at 6 stations distributed directly underneath the flight track and in lateral distances to the flight track. In this study, the 1/2 in condenser microphones were mounted inversely on a 400 mm diameter ground plate (see Fig.4) underneath the flight track according to International Civil Aviation Organization (ICAO) standard. The microphones are equipped with windscreens to suppress low frequency wind noise and record with a sampling rate of 48 kHz. The setup overfulfills the requirements for class 1 standards according to DIN EN 61672-1 [33]. The measurement uncertainty of the hardware lies within ± 1 dB. For wind speeds above 5 kts it

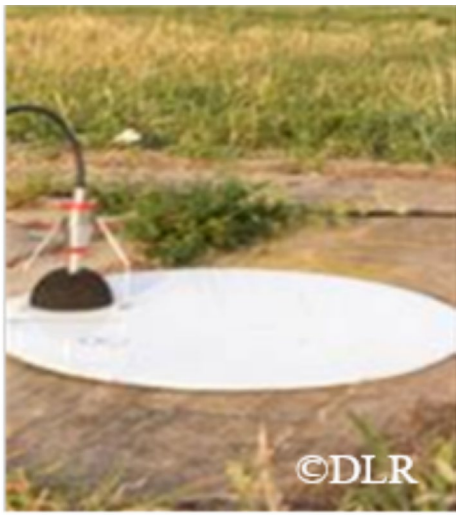

Fig. 4 Ground microphone with windscreen, inversely mounted on a ground plate, Credit: DLR (CC BY-NC-ND 3.0)

can rise up to ± 2 dB. However, tests were only conducted when the local weather conditions fulfilled the aircraft noise certification rules. From the recorded microphone's pressure data narrowband frequency spectra over a time span of 0.125 s were computed of which the integrated overall sound pressure level resulted in level-time histories which were corrected to the reference flight altitude of 500 ft accounting for geometrical spreading. Finally, 6 dB were subtracted from the sound pressure levels as an approximation to free-field conditions, according to DIN 45684-2 [34].

In addition to acoustic data, multiple metadata have been collected such as weather data, flight data of the onboard basic measurement system and of the inertial navigation system (INS), air data, and global positioning system (GPS) position and time. The GPS data also serve to synchronize the acoustic data and the aircraft related data. An additional ground based optical device enhanced the determination of the aircraft's height at the flyover point. More details about the test setup, the test matrix and further results can be found in [8].

5 Toolchain configuration

This work compares measurement and simulation of the whole aircraft, i.e., aircraft system noise. Therefore, all relevant noise sources of the aircraft are modeled. Depending on the source model, different inputs need to be pre-calculated. Following the path of the propeller noise modeling through the toolchain (see Fig.1), four steps are required until the final noise signal at the ground can be obtained:

1. Simulation of the propeller aerodynamics based on the current operating condition
2. Simulation of the acoustic sources of the propeller
3. Summation of the propeller noise and other aircraft noise sources
4. Propagation of the aircraft noise signature to the ground

The toolchain presented in section 3 is used to compute the propeller noise in both variants, with BEMT/Hanson (Fig.1) and with the external source model using UPM/APSIM (Fig.2). Depending on the variant, step 2) is either included in PANAM (Hanson) or executed external by APSIM.

5.1 Applied tools and methods

5.1.1 XFLR5

Xflr5 is developed by André Deperrois and Matthieu Scherrer [30]. The tool can be used for designing and analyzing the aerodynamics of airfoils, wings, and sails at low Reynolds numbers. It incorporates a C/C++ port of the commonly known XFOIL algorithms of Mark Drela and provides a graphical user interface. Two-dimensional airfoil analyses, analogous to those performed in XFOIL. Therefore, xflr5 re-implements the 2D panel method coupled to an integral boundary layer formulation of XFOIL. For three-dimensional configurations, xflr5 uses lifting-line, vortex-lattice and panel methods to calculate forces and static stability. The toolchain only uses the 2D analysis capabilities to compute the lift and drag polars required for the BEMT model.

5.1.2 QPROP

QPROP is a numerical tool developed by Mark Drela for analyzing the aerodynamic performance of propellers and wind turbines [35]. It uses the blade-element/vortex theory and calculates the forces and moments on individual blade sections. The blade-element/vortex theory is similar to the BEMT method, but uses the circulation bound to the propeller blade to estimate the induced velocities instead of the axial momentum. It features a radially-varying self-induced velocity, improving results for heavily loaded propellers. Hub- and tip loss effects are accounted for by an adapted method based on hub and tip loss factors, suggested by Prandtl and Glauert [36].

5.1.3 Hanson's helicoidal surface theory

Based on the acoustic analogy of Goldstein, Hanson developed a method to predict the sound pressure levels of rotating propellers [18] as a function of loading and thickness noise. The model includes the effect of forward flight and is

expressed in retarded coordinates. It considers the effect of blade geometry, namely blade sweep and lean on the phase shift of the pressure signal. Loading noise is estimated based on the load distribution of the blade at a certain operating condition. To simplify the input, the chordwise load distribution is estimated as constant over the chord length and only the radial load distribution available, e.g., from BET simulation is used. Furthermore, the chordwise thickness distribution is estimated as a quadratic function, which allows pre-computing the non-compactness effect. Both simplifications are suggested by Hubbard et al. [37].

5.1.4 PANAM

PANAM is a DLR tool used for assessing aircraft noise at the system level during the conceptual and preliminary design stages [27]. Originally, the tool was developed for turbofan aircraft, but it is under continuous development and recently extended to propeller application [10]. It uses parametrized, physics-based source models to compute standard metrics (e.g. $L_{A,max}$, SEL) along arbitrary three-dimensional trajectories. Interaction effects, such as installation and shielding, can be considered via external tools to enable realistic single-event and scenario evaluations. The tool was already validated for turbofan application [27] and compared to other aircraft noise prediction tools [38].

5.1.5 UPM

UPM is an unsteady free-wake panel method developed by DLR for simulating unsteady aerodynamic flows around moving bodies of arbitrary shape [39, 40]. Originally developed for helicopter applications, it can handle unsteady inflows and analyze aerodynamic interactions between propellers and wings. UPM is based on the assumption of inviscid, and irrotational flow with weak compressibility effect taken into account by Prandtl-Glauert compressibility factor. Lifting bodies are modeled using singularities defined by sources, sinks, and bound vortices to simulate displacement and lift. It features a non-linear, time-dependent free wake model and supports both vortex filament and vortex particle approaches for wake modeling (Fig. 5). The tool requires input of blade geometries with finite thickness and sharp trailing edges.

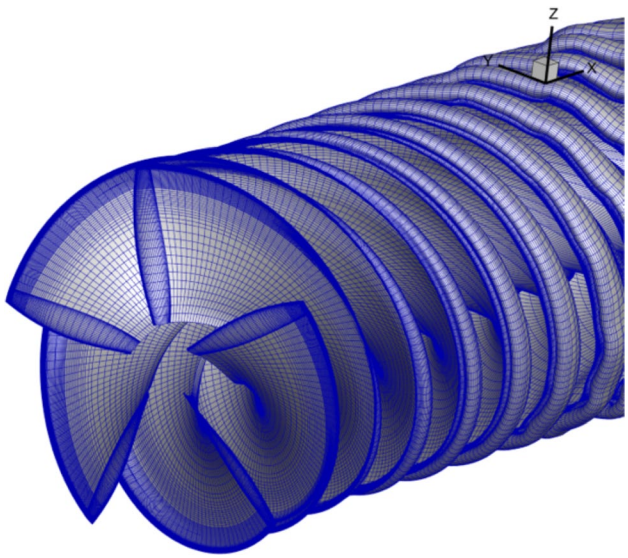

Fig. 5 Do 288 isolated propeller and wake computed with UPM using the vortex filament method (VFM) [10].

5.1.6 APSIM

APSIM is a computational tool developed for the prediction of rotor and propeller noise in the free field. It uses aerodynamic surface pressure data, typically provided by the UPM solver but also compatible with other aerodynamic codes, as input for the acoustic calculation.

The method is based on integral formulations of the FW-H equation, with the impermeable surface approach implemented using Farassat's 1 and 1A formulations [41]. Acoustic computations are performed in the time domain, where pressure distributions from the rotor blades serve as source terms.

Both loading noise, derived from the unsteady pressure distribution, and thickness noise, related to the displacement of fluid by the blades, are accounted for in the calculation. The resulting pressure time histories at arbitrary observer locations can be Fourier-transformed to obtain the corresponding acoustic spectra. APSIM can be applied to single or multiple rotors and provides the overall acoustic signature by combining all contributions.

5.2 Tool setup

5.2.1 PANAM setup and trajectory

The aircraft trajectory was recorded during the flyover measurements. This allows to replicate the measurement conditions as close as possible. The operating condition of the engine was measured in terms of engine torque and RPM. Both parameters were noted at the beginning of each flyover and held constant. The thrust required from PANAM was inferred for the current flight speed, torque and RPM from the manufacturer data.

Similar to the trajectories, the microphone positions were determined with GPS as well. All positional information are converted into a simple *xy*-coordinate system using a local transverse Mercator projection with the X-axis pointing north and the Y-axis pointing east. The microphones are

Table 1 List of airfoils used for the propeller blade model of the 5-bladed MTV-27 propeller ($R = 2.5m$) and the corresponding radial stations

r/R	Airfoil
0.25	MH126
0.50	MH112
0.75	MH114
0.95	MH116

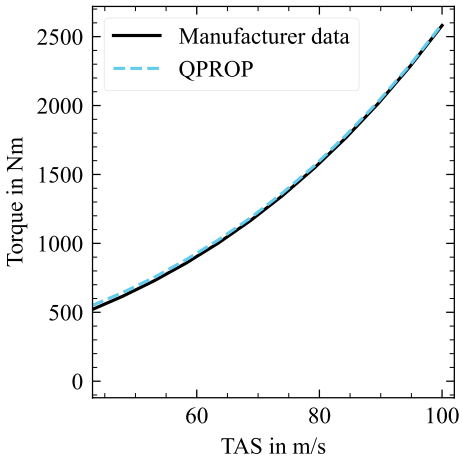

Fig. 6 Estimated torque of the BEMT model with QPROP in comparison to the manufacturer data. The propeller was trimmed to velocity dependent thrust setting derived from the flyover measurement data

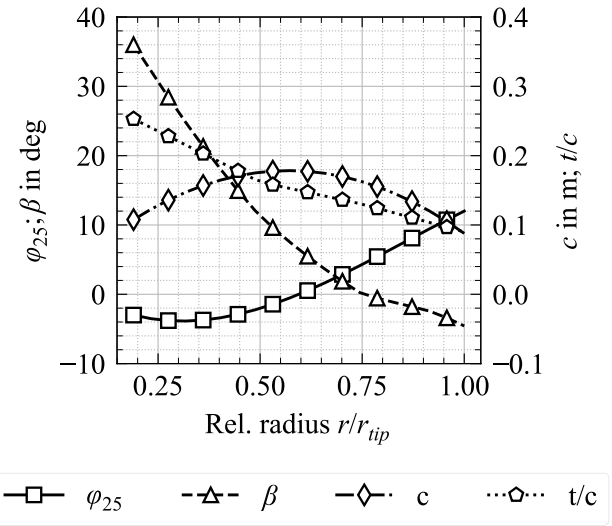

Fig. 7 Blade geometry parameters of the modeled propeller blade

modeled as free-field microphones to match the converted measurements.

The atmospheric conditions in PANAM are modeled with the SAE ARP 866 model [42]. The environment conditions are set to 50% humidity and 20°C air temperature, which is close to the average across all measurements.

5.2.2 QPROP model

The propeller blade of the 5-bladed MTV-27 propeller is remodeled with airfoils of Martin Hepperle (MH series) and the required lift and drag polars are computed with xflr5 at four different blade sections, listed in Table 1. The aerodynamic input is interpolated between these sections and the solution is computed at 30 equally spaced radial sections, providing a sufficiently resolved blade to replicate the manufacturers propeller performance data, as shown in Fig.6.

The radial variation of the blade geometry parameters quarter-chord sweep angle φ_{25}, blade pitch angle β, chord length c and thickness ratio t/c is plotted in Fig.7.

5.2.3 UPM

A 3D geometry is composed based on the geometry parameters from Table 1 and Fig.7. The blade is discretized into 40 chordwise panels on both the pressure and suction sides, and 30 spanwise panels. Panel density increases towards the tip to resolve tip vortex formation. This panel density was determined through a sensitivity study, as detailed by Manghnani [43]. A time step of 2.5° azimuth was used for simulating four complete propeller revolutions. Trailing edge Kutta conditions were enforced using a Neumann boundary condition, ensuring similar pressure gradients on the upper and lower surfaces. A tangential flow boundary condition was applied to the Kutta panels, eliminating the normal velocity component. With each time step, a quad-wake panel system was generated along the blade span, mirroring the spanwise panel distribution. This system utilized quad-wake filaments representing trailing and shed vortices, each with a vortex core diameter of 30% of the blade chord. The Kauffman-Scully vortex core model was implemented for vortex core representation [43].

The vortex filament method (VFM) was chosen for simulating isolated propeller configuration based on its accuracy and computational efficiency. A comparison between two different vortex method involving VFM and vortex particle method (VPM) is shown by Manghnani in [43]. A sensitivity study conducted by Manghnani [10] shows that for propeller in isolated configuration there is no difference in the noise levels observed on the acoustical far-field for VFM and VPM. The overall noise directivity remained unchanged, thus making vortex filament method more feasible and efficient for isolated propeller simulation.

The blade pitch at the root was calculated based on the geometric pitch specified at 75% span obtained from the BEMT simulations. This root pitch was then input into the UPM code to calculate blade loading.

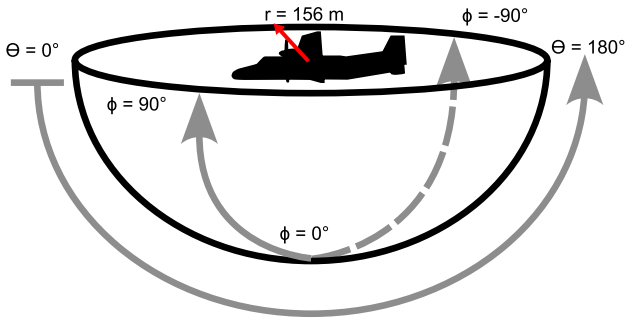

Fig. 8 Coordinate reference of the hemisphere used as the far-field receiver in APSIM [10]

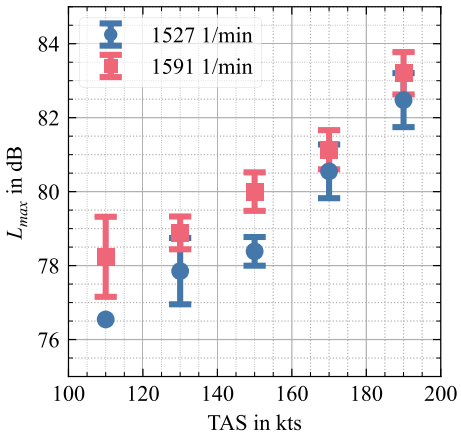

Fig. 9 Measured average L_{max} levels and standard deviation over airspeed for both RPM settings

5.2.4 APSIM

The far-field noise is computed on a hemisphere with a radius of 156 m as shown in Fig.8. This is the flyover altitude of #REC 77 and was used for all simulations, since the hemisphere is re-propagated to a 1 m radius hemisphere for PANAM anyway. The acoustic hemisphere is a far-field created by arranging virtual microphones in the form of hemisphere to capture noise from propeller installed configuration. The microphone grid has a spacing of 5°.

6 Results

6.1 Measurements

From the measured and processed level-time histories the average L_{max} values are determined from redundant measurements and plotted in Fig.9 versus the airspeed together with the standard deviations for the two rotational propeller speeds, i.e., 1527 1/min (96% RPM) and 1591 1/min (100% RPM). Overall, the maximum sound pressure levels increase with increasing airspeed. The values range from 76.5 dB to 82.5 dB for the cases of 96% RPM, and from 78.2 dB to 83.2 dB for the cases of 100% RPM. The values for the higher RPM thereby exceed the values for the lower RPM with higher differences (maximum 1.7 dB) found for the lower airspeeds and lower differences (minimum 0.7 dB) found for the higher airspeeds. It should be noted, however, that standard deviations of up to ± 1.4 dB are present in the data.

Table 2 Operating conditions at the 96% RPM setting (1527 1/min) with QPROP results

	110 kts flyover	190 kts flyover
RECORD #	67	71
TAS	53.0 m/s	95.2 m/s
T_{prop}	2201 N	3817 N
Q_{prop}	857 Nm	2539 Nm
η_{prop}	85.1%	89.4%
J	0.83	1.50
r/R at $T_{rel,max}$	0.65	0.85
r/R at $Q_{rel,max}$	0.67	0.85

Table 3 Operating conditions at the 100% RPM setting (1591 1/min) with QPROP results

	110 kts flyover	190 kts flyover
RECORD #	77	72
TAS	56.6 m/s	97.7 m/s
T_{prop}	2087 N	3881 N
Q_{prop}	825 Nm	2539 Nm
η_{prop}	85.4%	89.7%
J	0.85	1.47
r/R at $T_{rel,max}$	0.64	0.85
r/R at $Q_{rel,max}$	0.66	0.84

6.2 Blade loading

Blade loading is computed at four different operating conditions in total. Two different RPM settings are used, i.e. 1527 1/min (96%) and 1591 1/min (100%) with a slow (110 kts) and fast (190 kts) flyover. For each operating condition, one specific case was selected from the available data set [8] for a detailed analysis. The exact operating conditions are listed in Tables 2 and 3, respectively. Notably, the target velocities are not perfectly matched, which also influences the advance ratio J. The actual measured true air speed (TAS) for each case at the reference position is provided as well.

Figure 11 compares the normalized radial thrust distribution dT/dt for the selected cases calculated from the c_l and c_d distributions obtained from QPROP as

$$\frac{dT}{dr} = \frac{1}{2}\,\rho\,W^2\,c\,B\,\left[c_l\cos\phi - c_d\sin\phi\right], \tag{1}$$

$$\frac{dQ}{dr} = \frac{1}{2}\,\rho\,W^2\,c\,B\,r\,\left[c_l\sin\phi + c_d\cos\phi\right], \tag{2}$$

with density ρ, resulting velocity at the blade section W, chord length c, the number of blades B, and inflow angle ϕ calculated from the axial velocity at the blade W_a and the resulting velocity W (compare Fig.10) as

$$\phi = \arctan\left(\frac{W_a}{\sqrt{W^2 - W_a^2}}\right). \tag{3}$$

For better data handling, the load distributions are fitted with a 6-th order polynomial to import them into PANAM and normalized with the total thrust T and torque Q of the propeller blade, as required by the model of Hanson. To avoid non-physical results, the polynomials are only evaluated within the scope of the fitted data. Torque distributions are not compared, because they behave similarly to the thrust distributions (compare Tables 2 and 3) and are of less importance to the noise emission because of the overall lower surface forces.

The thrust distributions calculated by QPROP have a similar parabolic shape for all four cases, which is symmetrical to the loading peak and only located at a different radius. Comparing both RPM settings (diamond marker vs. square marker) shows a significant shift of the radial position of the respective maximum loading. For a flight speed of 110 kts, thrust peaks at around 65% of the radius. With increased flight speed, the loading peak moves further outward on the blade. At 190 kts, thrust peaks at approximately 85% of the blade radius. Furthermore, the comparison shows no significant differences between both RPM settings. At lower flight speeds, where the propeller tip speed is more influenced by the rotational speed, the load is shifted slightly towards a larger radius, while at a flight speed of 190 kts no differences in loading can be observed (Fig. 11).

The thrust distributions of UPM do not look as similar, as the thrust distributions of QPROP. All four cases show an asymmetric shape, much more focused towards the outside of the blade. Therefore, the blades are less loaded at the root and more towards the tip. This also leads to a steeper decline in thrust at the very blade tip and a larger maximum peak, compared to the results of QPROP.

6.3 Source comparison

The load distribution from QPROP is used to assess the effect of the radial load peak because it retains a similar shape

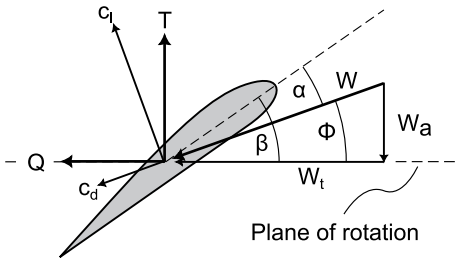

Fig. 10 Blade geometry and velocity triangle at one r location, adapted from [35]

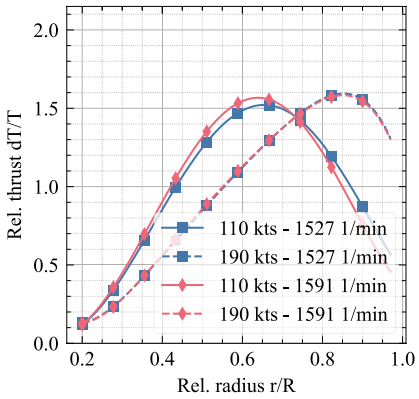

(a) QPROP

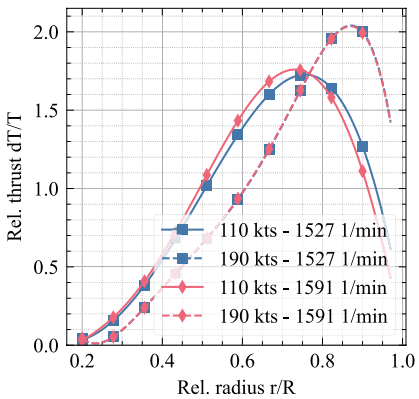

(b) UPM

Fig. 11 Comparison of radial blade loading distributions of the propeller computed with QPROP and UPM. The figures show the relative thrust (dT/T) versus the normalized blade radius (r/R) for both RPM settings. The thrust distributions are compared for flight speeds of 110 kts and 190kts

across the four operating conditions, varying mainly in the peak position. For clarity, the loading at 110 kts is denoted as *Load A* peak and that at 190 kts as *Load B*. The influence of blade loading on source-level noise is examined.

For each operating condition two simulations were performed: one with the blade loading corresponding to the current flight speed and one with the loading from the other flight speed. This procedure was applied separately for the two rotational-speed settings. In each case the thrust

matched the flight speed, while only the non-dimensional load distribution was swapped, allowing arbitrary thrust conditions to be tested independently of the load shape.

Thickness and loading noise are calculated separately using Hanson's model. The noise is simulated for the time step of to the L_{max} during the flyover. Figure 13 compares the influence of the different loadings, i.e., Load A and Load B, for $1527\,1/\mathrm{min}$ and Fig.14 for $1591\,1/\mathrm{min}$. The source noise is simulated for an isolated propeller on a semicircle ranging from $\Theta = 0°$ at the front to $\Theta = 180°$ at the back of the propeller, as shown in Fig.12. The noise is computed at a radius of $1\,\mathrm{m}$.

Figure 13 shows that changing the radius of the peak loading has only minor effects on noise emission. At low flight speeds (Fig.13 left), the propeller is only lightly loaded and loading noise contribution is lower than thickness noise. Especially towards the front the propeller mostly emits thickness noise, which reaches its maximum at $113.9\,\mathrm{dB}$ and $\Theta = 76°$. Moving the loading peak from 65 to 85% increases noise by $2\,\mathrm{dB}$, from $109.7\,\mathrm{dB}$ ($110\,\mathrm{kts}$ - Load A REC #67) to $111.7\,\mathrm{dB}$ ($110\,\mathrm{kts}$ - Load B REC #67). The emission angle of the maximum loading noise is only marginally influenced by moving the radial loading peak. It moves slightly towards the back from $\Theta = 92°$ to $\Theta = 94\circ$. The total noise of the propeller increases only slightly from $115.2\,\mathrm{dB}$ to $115.6\,\mathrm{dB}$, because thickness noise dominates. At higher flight speeds (Fig.13 right) the influence of moving the radial loading peak is similar, but slightly less pronounced. Here, the maximum loading noise increases from $120.2\,\mathrm{dB}$ ($110\,\mathrm{kts}$ - Load A REC #71) to $122.0\,\mathrm{dB}$ ($190\,\mathrm{kts}$ - Load B REC #71).

Therefore, the higher flight speed and thrust conditions increase loading noise by about $10\,\mathrm{dB}$ (Load B REC #67 vs. Load B REC #71). The corresponding emission angle moves forward due to the Doppler effect to $\Theta = 80°$, independent from the loading. Thickness noise increases as well, but only from $113.9\,\mathrm{dB}$ at $110\,\mathrm{kts}$ to $117.2\,\mathrm{dB}$ at $190\,\mathrm{kts}$, i.e., by $3.3\,\mathrm{dB}$. This leads to a dominant loading noise at high flight speeds, where the propeller has to produce more thrust to counter the aircraft drag, hence is higher loaded. Consequently, total propeller noise increases from $121.8\,\mathrm{dB}$ to $122.9\,\mathrm{dB}$.

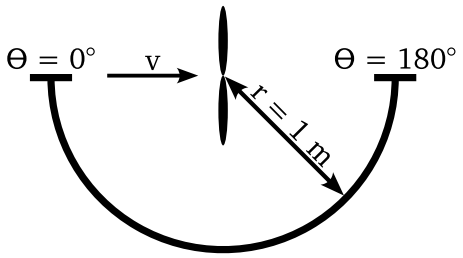

Fig. 12 Visualization of the source noise simulation setup

Comparing Figs.13 and 14 shows that the influence of propeller rotational speed is minor. The effect at low flight speeds is stronger at the higher RPM setting. Here, the difference between the 65% peak and the 85% peak is $2.2\,\mathrm{dB}$, compared to $1.9\,\mathrm{dB}$ at the lower RPM setting. Here, the thrust peak at $110\,\mathrm{kts}$ lies slightly more inboard (64%) compared to the low RPM case (65%).

In summary, moving the source peak from 65 to 85% of the blade radius, increases the loading noise by $2\,\mathrm{dB}$. Especially at $110\,\mathrm{kts}$, where thickness noise is dominant, the effect on the total noise emission is negligible. With increasing flight speed loading noise gains importance, although the impact of the moved loading peak reduces. At $190\,\mathrm{kts}$ the loading noise surpassed thickness noise and is

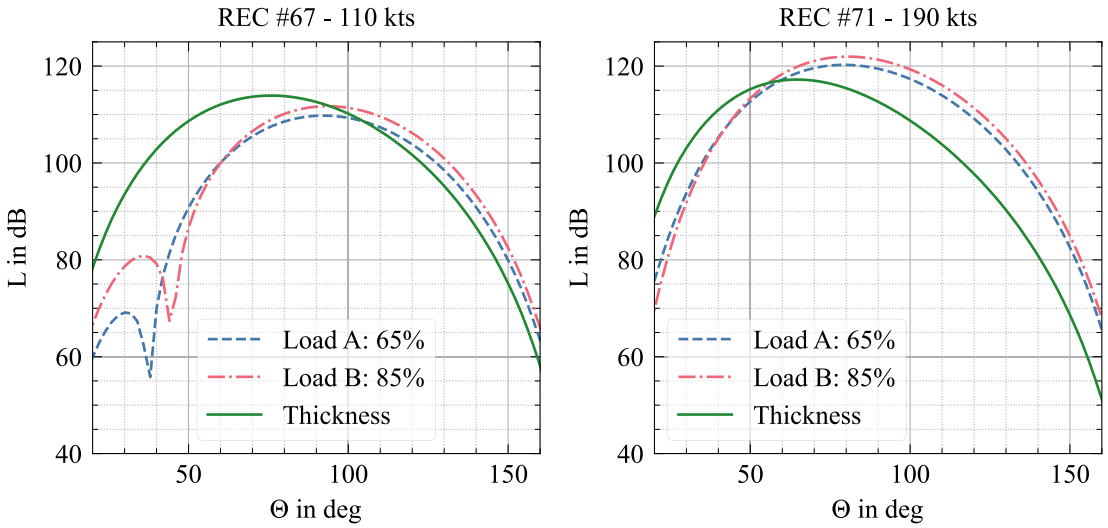

Fig. 13 Comparison of unweighted loading and thickness noise levels at $1\,\mathrm{m}$ radius for different blade loadings differing in peak radius. Two distinct flight speeds are compared ($110\,\mathrm{kts}$ and $190\,\mathrm{kts}$) for a rotational speed of $1527\,1/\mathrm{min}$

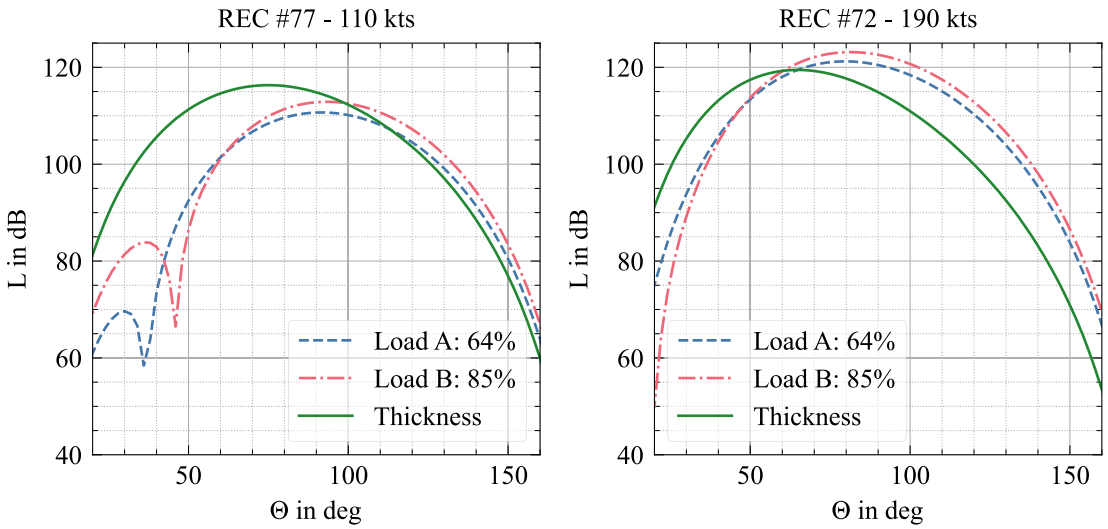

Fig. 14 Comparison of unweighted loading and thickness noise levels at 1 m radius for different blade loadings differing in peak radius. Two distinct flight speeds are compared (110 kts and 190 kts) for a rotational speed of 1591 1/min

the dominating source. Therefore, the influence on the total propeller noise increases to 1.2 dB. Nevertheless, total noise is still less influenced than loading noise alone, because of the additional thickness noise contributing to the total noise.

6.4 Flyover noise levels Measurement vs. Simulation

The measurement results in Fig.9 show that the received maximum levels increase with flight speed and RPM. These trends must be reproduced accurately by the toolchain. To evaluate this, simulated and measured ground-level L_{max} are compared for both RPM settings and for low (110 kts) and high (190 kts) flight speeds in Fig. 15. For each operating condition a representative test point is selected from the dataset in [8] (see Tables 2 and 3). Noise is simulated only for microphone position 1, because the results are almost identical for both microphone positions. To reduce the influence of uncontrolled environmental variability, the simulated values are compared with the overall averaged measurements shown in Fig.9. In addition to Hanson's model, levels are also simulated with the source model APSIM, using the higher-fidelity aerodynamic results from UPM (Fig.2).

Similar to the measurement evaluation, maximum noise levels are compared. Overall, simulation captures the velocity dependency of the sound pressure level well, but levels are consistently lower predicted than the experimental data by approximately 3 dB to 5 dB. The velocity trend is evaluated in Table 4 as $L_{max,190} - L_{max,110}$. The measured L_{max} increases by 5.9 dB at 1527 1/min and 5.0 dB at 1591 1/min. Hanson's model predicts a stronger increase by 6.6 dB and 7.1 dB respectively. The levels at 110 kts show a stronger underprediction compared to the levels at 190 kts. APSIM on the other hand, predicts with 5.2 dB a smaller increase in noise for 1527 1/min but, similar to Hanson's model, a larger increase by 6.1 dB for 1591 1/min.

Due to the small change in propeller rotational speed, the effect of RPM is difficult to assess. Yet, the comparison between experiment and simulations shows a favorable trend for the model of Hanson. It consistently predicts lower levels for 1527 1/min compared to 1591 1/min. At 110 kts the levels increase by 0.5 dB from the lower to the higher RPM setting, and at 190 kts by 1 dB. Similarly, the measured levels increase with higher RPM as well, by 1.7 dB at 110 kts and 0.7 dB at 190 kts. In contrast, APSIM predicts higher levels at 1527 1/min than at 1591 1/min.

7 Discussion

The comparison of the load distributions of QPROP and UPM in Fig.11 shows a substantial shift in the peak of the load distribution when the flight speed is increased from 110 kts to 190 kts and only a small impact of the change in rotational speed for both tools. Considering the results of [12] it can be deduced that this is mostly an effect of inflow velocity, but less of the applied thrust. The only significant difference between the two tools is observed in the shape of the thrust distribution. This can be attributed to the modelling of the blade-tip vortices and the effect on the induced velocity. QPROP uses Prandtl's hub and tip loss correction to model the effect of a finite blade, while UPM fully resolves the blade-tip (and hub) vortex.

The effect of shifting the loading peak from 65 to 85% on noise emission turns out to be comparable small in contrast

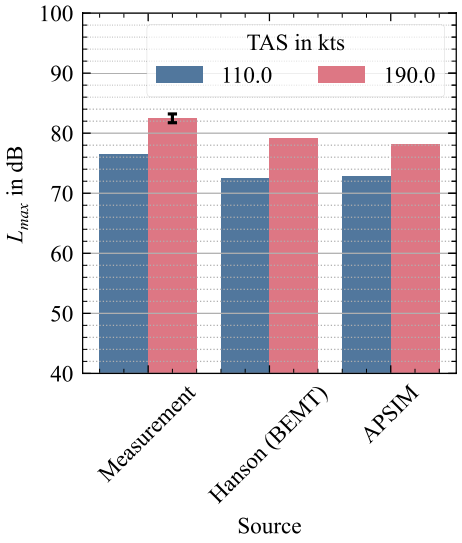

(a) 1527 1/min

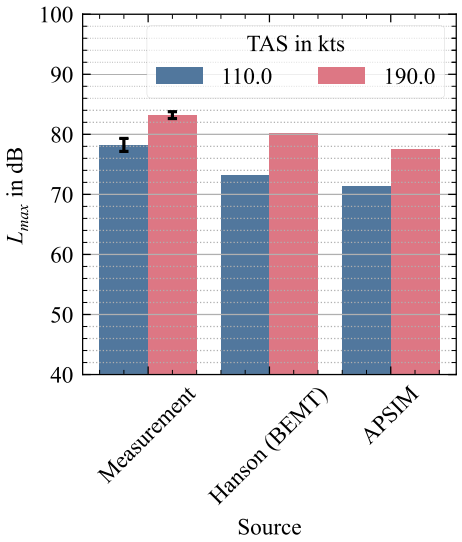

(b) 1591 1/min

Fig. 15 Flyover noise at 1527 1/min and 1591 1/min, with bars indicating averaged measurement data including the standard deviation and simulations. Simulation data is shown for a selected record of each operating condition only

Table 4 ΔL_{max} in dB between high flight speed (190 kts) and low flight speed (110 kts) for both RPM settings

RPM (1/min)	Measurement	Hanson	APSIM
1527	5.9	6.6	5.2
1591	5.0	7.1	6.1

to a similar shift using the effective radius assumption [9], which is in the order of 10 dB. Loading noise increases on average by about 2 dB, which is at a similar order as the results of Succi [23]. This effect is slightly larger at low flight speeds as at higher flight speeds. The effect on total noise contribution is further reduced by the additional thickness noise and independent of the rotational speed. The smaller impact of shifting the radial peak of a loading distribution compared to shifting the effective radius results from the large amount of blade loading unaffected by this shift. The effective radius moves the total applied load to a different radius. At low flight speeds Hanson's model predicts that thickness noise dominates, which is unusual and may result from the simplified thickness distribution employed [13, 37, 44].

Comparing the measured levels on ground to the simulation shows a constant underprediction of noise levels. Since the influence of the load distribution has only a small influence on the noise emission, an incorrect prediction of the blade loading can be ruled out as the main reason for this discrepancy. Similar trends were also found by Yunus et al. [25]. They identified unsteady loading noise as important factor for a correct prediction of the ground noise levels. Unsteady loading noise is not modeled in the current version of the toolchain. Therefore, this could cause the underprediction in this comparison. Unsteady loading can be introduced by a non-zero inflow angle, or by installation effects and has to be further investigated. Additionally, the propeller geometry is only approximated and results might differ from the actual propeller geometry. Finally, propeller noise is strongly influenced by environmental conditions, especially wind. Although measurement conditions were within the limits of DIN 45684-2 [34], to determine exact operating conditions is challenging, if not impossible.

At the moment, the cause of the over all lower levels of APSIM are unknown. Manghnani et al. [10] showed that directivity between Hanson's model and APSIM differs. This can lead to a larger distance between the aircraft and the microphone when the maximum level is reached, resulting in a lower L_{max}. Following the results of this study, the different radial blade loading does not cause the lower levels but other than the Hanson model, APSIM also considers the chordwise loading and thickness, which can influence the emitted noise [13, 37].

8 Summary and conclusion

This work employs a newly developed toolchain for predicting propeller-aircraft noise under various operating conditions. The toolchain results are benchmarked against higher-fidelity methods and measurement data, and the influence of a shifting loading peak is examined.

The toolchain is intended for integration into existing frameworks and preliminary-design optimization loops. Hanson's model provides the noise source, requiring radial blade loadings from a BEMT solver. Results are compared

with fly-over measurements and the external source model APSIM.

The evaluation of the measurement data reveals that maximum sound pressure levels rise with increasing airspeed and rotational speed. Flight speed significantly influences the radial position of the thrust peak, shifting it outward from approximately 65% of the radius at 110 kts to 85% at 190 kts. Both QPROP and UPM predict this trend, though UPM's radial load distribution is more concentrated near the blade tip.

The effect of varying the loading peak from 65 to 85% of the blade radius is relatively minor, increasing loading noise by only 2 dB with minor dependencies on operating conditions. Hence, a single representative load distribution can be used as a good approximation to model an entire trajectory for landing and takeoff. Simulation results consistently underpredict noise levels by approximately 3 dB to 5 dB compared to experimental data. Hanson's model generally predicts higher levels than APSIM, but both models accurately capture the overall velocity trend. This is most important for the correct prediction of landing and takeoff noise, where flight speeds vary significantly. However, neither model successfully replicates the impact of propeller RPM. Therefore, combining BEMT with Hanson's model provides a practical prediction approach. Employing higher-fidelity methods does not substantially improve prediction accuracy for the selected applications cases.

In the near future this simulation process is foreseen to enable low-noise design of novel vehicles and technologies. Initial work towards this goal is presented in [9]. Furthermore, the influence of unsteady loading noise and angle of attack will be investigated and implemented into the process.

Author contributions V.D. wrote the main manuscript text and prepared all figures. A.F.-H. wrote sections 4 and 6.1. J.M. wrote sections 5.1.5, 5.1.6, 5.2.3, and 5.2.4. All authors reviewed the manuscript.

Funding Open Access funding enabled and organized by Projekt DEAL. The authors gratefully acknowledge the scientific support and HPC resources provided by the German Aerospace Center (DLR). The HPC system CARA is partially funded by "Saxon State Ministry for Economic Affairs, Labour and Transport" and "Federal Ministry for Economic Affairs and Climate Action". The HPC system CARO is partially funded by "Ministry of Science and Culture of Lower Saxony" and "Federal Ministry for Economic Affairs and Climate Action".

Data availability No datasets were generated or analysed during the current study.

Declarations

Conflict of interest The authors declare no conflict of interest.

References

1. Europäische Kommission: Flightplan 2050: Europe's Vision for Aviation; Maintaining Global Leadership and Serving Society's Needs; Report of the High-level Group on Aviation Research. policy. Publ. Off. of the Europ. Union, Luxembourg (2011)
2. Wehrspohn, J., Rahn, A., Papantoni, V., Silberhorn, D., Burschyk, T., Schröder, M., Linke, F., Dahlmann, K., Kühlen, M., Wicke, K., Wende, G.: A detailed and comparative economic analysis of hybrid-electric aircraft concepts considering environmental assessment factors. In: AIAA AVIATION 2022 Forum. American Institute of Aeronautics and Astronautics, Reston, Virginia (2022). https://doi.org/10.2514/6.2022-3882
3. Atanasov, G., Wehrspohn, J., Kühlen, M., Cabac, Y., Silberhorn, D., Kotzem, M., Dahlmann, K., Linke, F.: Short-medium-range turboprop-powered aircraft as a cost-efficient enabler for low climate impact. In: AIAA AVIATION 2023 Forum. American Institute of Aeronautics and Astronautics, Reston, Virginia (2023). https://doi.org/10.2514/6.2023-3368
4. Schmid, R.: Entwicklung der Fluglärmsituation in Deutschland im 21. Jahrhundert - FLUID-21 - Projektleiterbericht, Göttingen, Germany. https://elib.dlr.de/202637/
5. Schmid, R., Blinstrub, J., Gelhausen, M., Grimme, W., Kurz, J., Schmitz, G., Bartels, S.: Dlr-projekt fluid-21 - entwicklung der fluglärmsituation in deutschland von der jahrtausendwende bis zur mitte des 21. jahrhunderts. In: Peissig, J., Rolfes, R. (eds.) Fortschritte der Akustik - DAGA 2024. Deutsche Gesellschaft für Akustik e.V. (DEGA), Berlin, Germany (2024). https://elib.dlr.de/202336/
6. Kryter, K.D.: The meaning and measurement of perceived noise level. Noise Control **6**(5), 12–27 (1960). https://doi.org/10.1121/1.2369423
7. Isermann, U., Bertsch, L.: Aircraft noise immission modeling. CEAS Aeronaut. J. **10**(1), 287–311 (2019). https://doi.org/10.1007/s13272-019-00374-5
8. Feldhusen-Hoffmann, A., Bertsch, L., Pott-Pollenske, M., Domogalla, V., Kreienfeld, M., Doerge, N.: Noise and local pollutants of small aircraft: overview of simulation activities and of the first flight test within the DLR project L2INK. In: AIAA AVIATION 2023 Forum. American Institute of Aeronautics and Astronautics, Reston, Virginia (2023). https://doi.org/10.2514/6.2023-4171
9. Hon, K.S., Domogalla, V., Feldhusen-Hoffmann, A., Blinstrub, J., Bertsch, L., Snellen, M., Zill, T., Angermann, M.: Development of a simulation process for conceptual cs-23 propeller aircraft system noise assessment. In: AIAA AVIATION FORUM AND ASCEND 2025. American Institute of Aeronautics and Astronautics, Reston, Virginia (2025). https://doi.org/10.2514/6.2025-3365
10. Manghnani, J., Domogalla, V., Ewert, R., Bertsch, L., Delfs, J.W.: A first principle based approach for prediction of tonal noise from isolated and installed propeller. In: 30th AIAA/CEAS Aeroacoustics Conference (2024). American Institute of Aeronautics and

Astronautics, Reston, Virginia (2024). https://doi.org/10.2514/6.2024-3382
11. Gutin, L.: On the sound field of a rotating propeller: Translated 1948 as naca-tm-1195. Physikalische Zeitschrift der Sowjetunion **9**(1) (1936)
12. Nallasamy, M., Woodward, R.P., Groeneweg, J.F.: High-speed propeller performance and noise predictions at takeoff/landing conditions. J. Aircr. **26**(6), 563–569 (1989). https://doi.org/10.2514/3.45803
13. Hanson, D.B.: Influence of propeller design parameters on far-field harmonic noise in forward flight. AIAA J. **18**(11), 1313–1319 (1980). https://doi.org/10.2514/3.50887
14. Farassat, F., Succi, G.P.: A review of propeller discrete frequency noise prediction technology with emphasis on two current methods for time domain calculations. J. Sound Vib. **71**(3), 399–419 (1980). https://doi.org/10.1016/0022-460X(80)90422-8
15. Ffowcs Williams, J.E., Hawkings, D.L.: Sound generation by turbulence and surfaces in arbitrary motion. Philosophical transactions of the royal society of London. Series A. Math. Phys. Sci. **264**(1151), 321–342 (1969). https://doi.org/10.1098/rsta.1969.0031
16. Glegg, S., Devenport, W.: Aeroacoustics of Low Mach Number Flows: Fundamentals, Analysis, and Measurement. Academic Press, London (2017)
17. Hanson, D.B., Fink, M.R.: The importance of quadrupole sources in prediction of transonic tip speed propeller noise. In: Spring Meeting of the Institute of Acoustics (1978). https://ntrs.nasa.gov/api/citations/19780024890/downloads/19780024890.pdf
18. Hanson, D.B.: Helicoidal surface theory for harmonic noise of propellers in the far field. AIAA J. **18**(10), 1213–1220 (1980). https://doi.org/10.2514/3.50873
19. Hanson, D.B., Parzych, D.J.: Theory for Noise of Propellers in Angular Inflow with Parametric Studies and Experimental Verification, Cleveland, OH, United States. https://ntrs.nasa.gov/citations/19930015905
20. Bergmann, O., Möhren, F., Braun, C., Janser, F.: Comparison of various aeroacoustic propeller noise prediction methodologies in static operations. In: AIAA SCITECH 2022 Forum. American Institute of Aeronautics and Astronautics, Reston, Virginia (2022). https://doi.org/10.2514/6.2022-2529
21. Zawodny, N.S., Boyd, D. Douglas, Jr., Burley, C.L.: Acoustic characterization and prediction of representative, small-scale rotary-wing unmanned aircraft system components. In: American Helicopter Society (ed.) AHS International 72nd Annual Forum & Technology Display (2016). https://doi.org/10.4050/F-0072-2016-11346 . https://ntrs.nasa.gov/citations/20160009054
22. Hambrey, J., Kotwicz Herniczek, M., Feszty, D., Meslioui, S.-A., Park, J.: Comparison of three popular methods for the prediction of high speed propeller noise. In: 23rd AIAA/CEAS Aeroacoustics Conference. American Institute of Aeronautics and Astronautics, Reston, Virginia (2017). https://doi.org/10.2514/6.2017-4181
23. Succi, G.P.: Design of quiet efficient propellers. In: SAE Technical Paper Series. SAE Technical Paper Series. SAE International, Warrendale, PA, United States (1979). https://doi.org/10.4271/790584
24. Miller, C.J., Sullivan, J.P.: Noise Constraints Effecting Optimal Propeller Designs, Cleveland, OH, United States. https://ntrs.nasa.gov/citations/19850011613
25. Yunus, F., den Hoff, B., Snellen, M.: Predicting tonal noise of full-electric propeller-driven aircraft in outdoor environments using low-order models. In: 30th AIAA/CEAS Aeroacoustics Conference (2024). American Institute of Aeronautics and Astronautics, Reston, Virginia (2024). https://doi.org/10.2514/6.2024-3418
26. Grande, E., Massarino, C., Kroemer, F., Feigel, A., Aquilini, C.: Aeroacoustic study of a twin-turboprop aircraft using the lattice-boltzmann method. In: Proceedings of the 10th Convention of the European Acoustics Association Forum Acusticum 2023, pp. 3857–3863. European Acoustics Association, Turin, Italy (2024). https://doi.org/10.61782/fa.2023.0329
27. Bertsch, L.: Noise prediction within conceptual aircraft design. Dissertation, Technischen Universität Carolo-Wilhelmina zu Braunschweig, Braunschweig (13.08.2013). https://doi.org/10.34912/n0is3-d3sign . https://elib.dlr.de/84386/
28. Blinstrub, J.: Immission-based noise reduction within conceptual aircraft design. Dissertation, Technischen Universität Carolo-Wilhelmina zu Braunschweig, Braunschweig (2019). https://elib.dlr.de/127483/
29. Alder, M., Moerland, E., Jepsen, J., Nagel, B.: Recent advances in establishing a common language for aircraft design with cpacs. In: Aerospace Europe Conference 2020 (2020). https://elib.dlr.de/134341/1/AEC2020_174.pdf
30. Deperrois, A., Scherrer, M.: (2023). http://www.xflr5.tech/xflr5.htm
31. Gur, O., Rosen, A.: Comparison between blade-element models of propellers. Aeronaut. J. **112**(1138), 689–703 (2008). https://doi.org/10.13140/RG.2.1.3854.5129
32. Goyal, J., Sinnige, T., Ferreira, C., Avallone, F.: Effect of angle of attack on propeller aeroacoustics at positive and negative thrust. Journal of Aircraft, 1–21 (2025) https://doi.org/10.2514/1.C038073
33. DIN Deutsches Institut für Normung e.V.: Elektroakustik - Schallpegelmesser - Teil 1: Anforderungen. Beuth Verlag GmbH, Berlin, Germany (2014). https://doi.org/10.31030/2154580
34. DIN Deutsches Institut für Normung e.V.: Akustik - Ermittlung von Fluggeräuschimmissionen an Landeplätzen - Teil 2: Bestimmung akustischer und flugbetrieblicher Kenngrößen. Beuth Verlag GmbH, Berlin (2015). https://doi.org/10.31030/2359228
35. Drela, M., Youngren, H.: QPROP: Propeller/Windmill Analysis and Design. Massachusetts Institute of Technology (2007). https://web.mit.edu/drela/Public/web/qprop/
36. Durand, F. (ed.): Aerodynamic Theory: Vol. IV vol. 4. Julius Springer, Berlin (1935). https://doi.org/10.1017/S0368393100110363
37. Hubbard, H.H.: Aeroacoustics of Flight Vehicles: Theory and Practice. Volume 1: Noise Sources, Hampton, VA, United States (1991)
38. Bertsch, L., Sanders, L., Thomas, R.H., LeGriffon, I., June, J.C., Clark, I.A., Lorteau, M.: Comparative assessment of aircraft system noise simulation tools. J. Aircr. **58**(4), 867–884 (2021). https://doi.org/10.2514/1.C036124
39. Ahmed, S.R., Vidjaja, V.T.: Unsteady panel method calculation of pressure distribution on bo 105 model rotor blades. J. Am. Helicopter Soc. **43**(1), 47–56 (1998). https://doi.org/10.4050/JAHS.43.47
40. Yin, J., Le Chuiton, F., Schmid, M., Schwarz, T.: Dlr free wake unsteady panel method (upm): User guide. Technical report, Institute of Aerodynamics and Flow Technology, Braunschweig, Germany (2024)
41. Farassat, F.: Derivation of Formulations 1 and 1A of Farassat, Washington, D.C., United States. https://ntrs.nasa.gov/citations/20070010579
42. Society of Automotive Engineers (SAE): Standard Values of Atmospheric Absorption as a Function of Temperature and Humidity. Technical Report Aerospace Recommended Practice, SAE ARP 866A, SAE (1975)
43. Manghnani, J., Ewert, R., Delfs, J.: Towards data-driven aeroacoustic modeling to predict propeller installation noise: A first-principle based approach. In: AIAA Aviation Forum and ASCEND 2025. American Institute of Aeronautics and

Astronautics, Reston, Virginia (2025). https://doi.org/10.2514/6.2025-3220
44. Hanson, D.B.: Propeller noise caused by blade tip radial forces. In: 10th Aeroacoustics Conference. American Institute of Aeronautics and Astronautics, Reston, Virigina (1986). https://doi.org/10.2514/6.1986-1892